

Overcome Low Intrinsic Conductivity of NiO_x through Triazinyl Modification for Highly Efficient and Stable Inverted Perovskite Solar Cells

Jiabao Yang,^a Tong Wang,^a Yaohua Li,^b Xingyu Pu,^a Hui Chen,^a Yuke Li,^c Bowen Yang,^{d,e*} Yixin Zhang,^a Junsong Zhao,^a Qi Cao,^a Xingyuan Chen,^a Shahnaz Ghasemi,^f Anders Hagfeldt,^{d,e} Xuanhua Li^{a*}

^[a] State key Laboratory of Solidification Processing, Center for Nano Energy Materials, School of Materials Science and Engineering, Northwestern Polytechnical University, Xi'an 710072, People's Republic of China

*Email address: lixh32@nwpu.edu.cn

^[b] Yinchuan Branch, Taiyuan Satellite Launch Center, Yinchuan, 750000 China

^[c] Department of Chemistry and Centre for Scientific Modeling and Computation, Chinese University of Hong Kong, Shatin, Hong Kong 999077, China

^[d] Department of Chemistry-Ångström Laboratory, Uppsala University, SE-75120 Uppsala, Sweden

^[e] Laboratory of Photomolecular Science, Institute of Chemical Sciences and Engineering, School of Basic Sciences, Ecole Polytechnique Fédérale de Lausanne, CH-1015 Lausanne, Switzerland

^[f] Sharif Energy, Water and Environment Institute, Sharif University of Technology, Azadi Avenue, P.O.Box 11365-9465, Tehran, Iran

*Email address: bowen.yang@kemi.uu.se

Abstract

Nickel oxide (NiO_x) is a promising hole transport material in inverted organic-inorganic metal halide perovskite solar cells (PSCs). However, its low intrinsic conductivity hinders its further improvement in device performance. Here, we employ a trimercapto-s-triazine trisodium salt (TTTS) as a chelating agent of Ni²⁺ in the NiO_x layer to improve its conductivity. Due to the electron-deficient triazine ring, the TTTS complexes with Ni²⁺ in NiO_x via strong Ni²⁺-N coordination bond and increases the ratio of Ni³⁺: Ni²⁺. The increased Ni³⁺ concentration adjusts the band structure of NiO_x, thus enhancing

This article has been accepted for publication and undergone full peer review but has not been through the copyediting, typesetting, pagination and proofreading process, which may lead to differences between this version and the [Version of Record](#). Please cite this article as [doi: 10.1002/solr.202200422](https://doi.org/10.1002/solr.202200422).

hole density and mobility, eventually improving the intrinsic conductivity of NiO_x. As a result, the device with TTTS modification displays a champion PCE of 22.81%, 13.36% enhancement compared to the control device (20.12%). The encapsulated device based on modified-NiO_x layer maintains 94% of its initial power output at the maximum power point and continuous one-sun illumination for 1000 h at 45 °C. In addition, the unencapsulated target devices also maintain 92% at 60 ± 5% relative humidity and 25 °C in air for 5000 h; and 91% at 85 °C in a nitrogen atmosphere for 1000 hours. Our research provides an effective strategy to enhance PCE and stability of inverted PSCs via modifying NiO_x films with triazine molecule.

Keywords: nickel oxide, intrinsic conductivity, additive engineering, device stability, inverted perovskite solar cells

1. Introduction

The organic-inorganic metal halide perovskite solar cells (PSCs) have attracted extensive attention because of its low-cost solution preparation and outstanding power conversion efficiency (PCE).^[1-4] At present, the state-of-the-art traditional (n-i-p) PSCs have reached record PCE of 25.7%^[5]. Inverted PSCs have made great breakthroughs,^[6] but their PCE are still behind the traditional PSCs. The inverted PSCs display less hysteresis effect, better stability, and excellent compatibility with tandem cells.^[7] Around the inverted PSCs, the modifications of hole transport layer and its interface with perovskite have drawn tremendous attention.^[8-10]

Nickel oxide (NiO_x) has served as a promising hole transport layer because of its excellent stability and high optical transparency^[11]. However, NiO_x has relatively low intrinsic conductivity, which might be the main reason that limits its further improvement in PCE for inverted PSCs^[12]. So

far, metal ionic doping and additive engineering are proved as effective methods for modifying the NiO_x film. Metal ionic doping such as Li⁺^[13], Cs⁺^[14], Ag⁺^[15], Mg²⁺^[16], Cu²⁺^[17-19], Co²⁺^[20], Zn²⁺^[21] and Sm³⁺^[22] can effectively improve the conductivity of the NiO_x film. However, doping will create additional processes and unmanageable disorders or defects.^[23] Additive engineering, on the other hand, is a simple way to adjust the band structure and improve the conductivity of the NiO_x film via molecules such as 3,6-difluoro-2,5,7,8-tetracyano quinodimethane (F2HCNQ)^[23] and 2,2'-(perfluoronaphthalene-2,6-diylidene) dimalononitrile (F6TCNNQ)^[24]. Nevertheless, their mechanism of the increasement in the conductivity of NiO_x is still unclear.

Here, we employ trimercapto-s-triazine trisodium salt (TTTS) as an additive in the NiO_x layer to improve its intrinsic conductivity and understand its mechanism by combining experimental characterizations and theoretical calculations (see **Figure 1a**). We find that TTTS can act as a chelating agent, which complexes with heavy metal ions such as the Ni²⁺ in NiO_x, due to the three electron-rich sulfur ions and electron-deficient triazine ring. We also reveal that the ratio of Ni³⁺: Ni²⁺ is increased due to the strong Ni²⁺-N coordination bond between NiO_x and TTTS. The increased Ni³⁺ concentration adjusts the band structure of NiO_x, thus enhancing hole density and mobility, eventually improving the intrinsic conductivity. In addition, modification with TTTS is also beneficial to achieve better interface contact. As a result, the optimized device displays a champion PCE of 22.81% with excellent stabilities under various ageing conditions. Remarkably, the encapsulated device with NiO_x:TTTS layer still maintains 94% of its initial power output after continuous one-sun illumination at 45 °C for 1000 h under maximum power point tracking. In addition, the unencapsulated devices display 92% ambient stability at 60 ± 5% relative humidity (RH) and 25 °C in air for 5000 h; and 91% thermal stability at 85 °C in nitrogen for 1000 h.

2. Results and discussion

The architecture of PSCs prepared in this work is ITO (indium tin oxide) /NiO_x without or with TTTS /triple-cation perovskite (termed as CsFAMA) /PCBM:C₆₀ /BCP /Cr /Au (Cs is caesium, FA is formamidinium, MA is methylammonium, PCBM represents [6,6] -phenyl-C₆₁-butyric acid methyl ester, and BCP represents bathocuproine) in **Figure 1a**. To understand the interaction between NiO_x and TTTS, we perform the Fourier transform infrared spectroscopy (FTIR) in **Figure 1b and S1**. The stretching vibrations of C=N and C-N blue-shift to higher wavenumbers of 1636.4 and 1210.5 cm⁻¹ for the TTTS modified NiO_x film (termed as NiO_x:TTTS) compared with the peak at 1629.0 and 1200.1 cm⁻¹ for the TTTS film, respectively (**Figure 1b**). Similarly, the stretching vibrations of C-S bond blue-shift to higher wavenumbers of 851.3 cm⁻¹ for the NiO_x:TTTS film compared with the peak at 846.0 cm⁻¹ for the TTTS film (**Figure S1**). These results indicate that nitrogen (N) and sulfur (S) in TTTS have interactions with NiO_x.

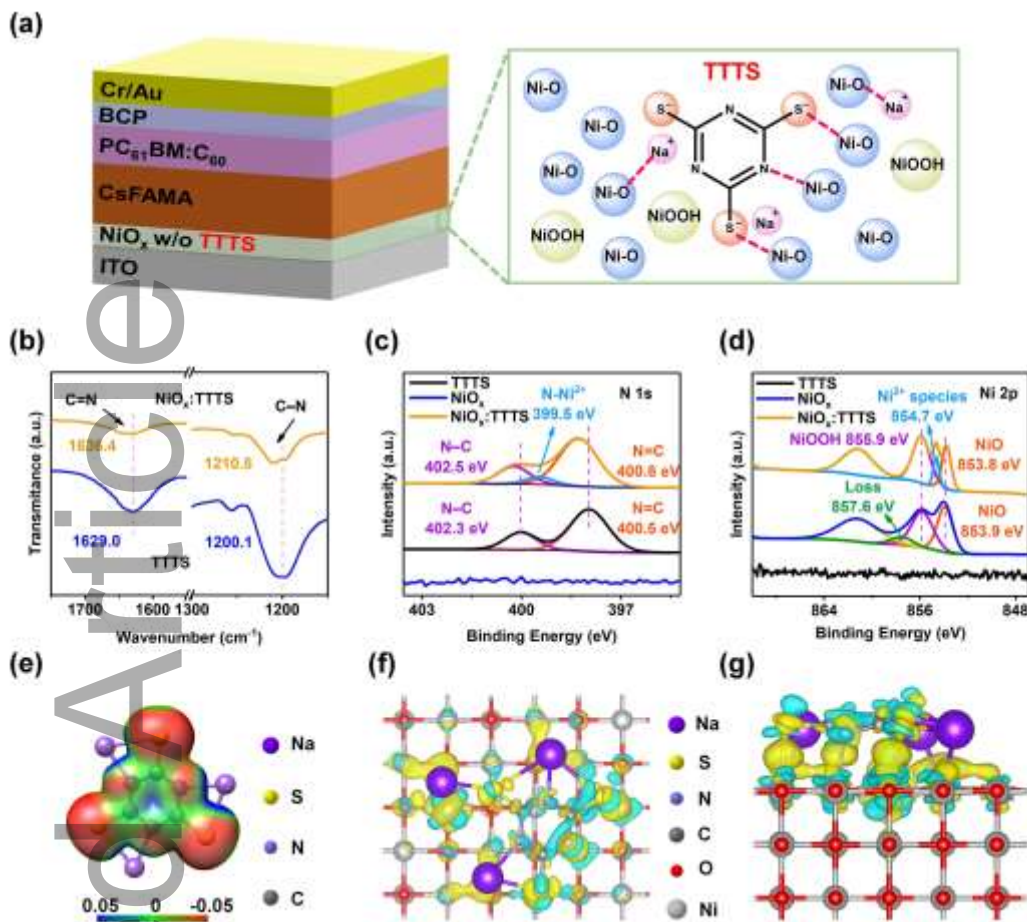


Figure 1. The mechanism analyses and theoretical calculation. (a) The structure of PSCs and the schematic diagram of the NiO_x layer modified with TTTS. (b) The enlarged FTIR spectra of C=N and C-N for TTTS and NiO_x :TTTS films. Deconvolution XPS spectra of (c) N 1s and (d) Ni 2p for TTTS, NiO_x film and NiO_x :TTTS film. (e) Electrostatic potential mesh maps of TTTS. The (f) top view and (g) side view of interfacial bonding interaction at the NiO_x /TTTS interfaces. The yellow color and blue color represent charge depletion and charge accumulation, respectively.

To further investigate these interactions, we conduct the X-ray photoelectron spectroscopy (XPS) analysis on TTTS, NiO_x , and NiO_x :TTTS films, as shown in **Figure 1c-d and S2**, respectively. The new peak in N 1s (399.5 eV, **Figure 1c**) are observed in the NiO_x :TTTS film, revealing the binding between the N atom in TTTS and the NiO_x , which is consistent with the FTIR result shown above. In addition, the two main peaks in N 1s at 402.3 and 400.5 eV designated as N-C and N=C bond shift to higher binding energies of 402.5 and 400.8 eV, respectively, indicating a decrease in the electron density near N atoms. **Figure 1d** depicts the Ni $2p_{3/2}$ spectrum, and the two main peaks at 855.9 and

853.9 eV of the NiO_x film, which are assigned to NiOOH and NiO, respectively.^[25] After modification with TTTS, no obvious peak shift for Ni³⁺ is observed, indicating that TTTS is not reacting with Ni³⁺. Therefore, we attribute the new peak located at 854.7 eV to the new Ni²⁺ species.^[26] Furthermore, we notice that the ratio of Ni³⁺: Ni²⁺ increases from 1.11 to 1.44 after TTTS modification, which is beneficial for the hole mobility and conductivity of NiO_x layer.^[14, 27] In addition, the new peaks in S 2p are observed at 162.7 and 161.3 eV (**Figure S2**), indicating a bond between S and Ni²⁺. The main peak of O²⁻ in NiO shifts to a lower binding energy, while the main peak of Na⁺ in TTTS shifts to a higher binding energy (**Figure S2**), revealing their potential interactions via electronic transfer.

To better understand the relationship of the interactions mentioned above and the ratio of Ni³⁺: Ni²⁺, we perform theoretical calculations to investigate interface charge transfer at atomic scale. **Figure 1e** depicts the electrostatic potential of TTTS, and there is local negative charge (red) around S atoms and positive charge (blue) around N atoms, respectively. We further calculate bonding interaction (**Figure 1f-g**) and charge transfer (**Figure S3**) at the NiO_x and TTTS interface via density functional theory. The Ni atom in NiO losses 0.05e when the Ni-N coordination bond is formed, leading to an increase in the ratio of Ni³⁺: Ni²⁺. It is worth noting that the decrease of electron density in N atoms is attributed to the strong electron-withdrawing triazine ring conjugation system with the N-C and N=C bonds. On the contrary, when the Ni-S bond is formed, the Ni atoms in NiO attain 0.1e, which is beneficial for charge transport.^[28] In addition, the O atom in NiO attains 0.07e via O-Na bond, which decreases reactive dangling bonds around the O atom and reduces defect density.^[29] To further clarify whether Na⁺ incorporates into the lattice of NiO_x, we perform the X-ray diffraction (XRD) patterns for NiO_x and NiO_x:TTTS films in **Figure S4**. There are the same diffraction peaks

for the NiO_x films without or with TTTS and their positions are not shifted, revealing Na^+ is not doped in NiO lattice.

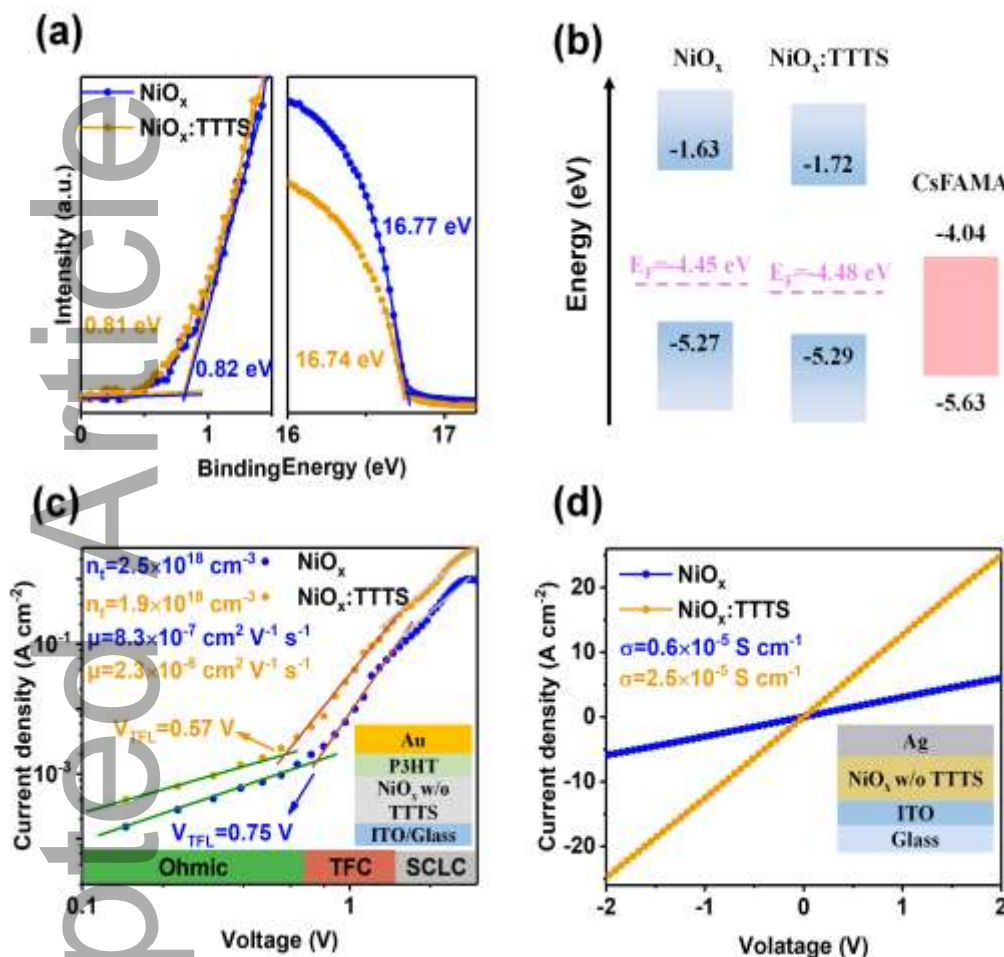


Figure 2. The band alignment and electrical effect of TTTS on NiO_x layer. (a) The UPS spectra of NiO_x and $\text{NiO}_x:\text{TTTS}$ films (b) The electronic energy level diagram of NiO_x and $\text{NiO}_x:\text{TTTS}$ layers. (c) Dark J - V characterization of the NiO_x and $\text{NiO}_x:\text{TTTS}$ films. The inset is the device structure with ITO / NiO_x without or with TTTS /P3HT/Au. (d) The conductivity measurement of NiO_x and $\text{NiO}_x:\text{TTTS}$ films. The inset is the device structure with ITO / NiO_x without or with TTTS /Ag. P3HT is poly(3-hexylthiophene) polymer.

In order to clarify the effect of the increased concentration of Ni^{3+} on the energy band structure of NiO_x , we conduct the Tauc plots of $(\alpha h\nu)^2$ versus $h\nu$ characterizations (**Figure S5**) and ultraviolet photoelectron spectroscopy (UPS, **Figure 2a**), then depict the electronic energy level diagram in **Figure 2b**. The lower E_F and VBM can achieve better band alignment and hole extraction, which is beneficial for enhancement of V_{OC} . Moreover, the decrease of $\text{NiO}_x:\text{TTTS}$ film in the energy gap

This article is protected by copyright. All rights reserved

($\Delta E_V = E_F - E_V$) with comparison to the NiO_x film reveals an enhanced hole density (1.47 times). The hole density (p) can be calculated from the formula^[28]:

$$p = N_V \exp\left(\frac{-\Delta E_V}{k_B T}\right) \quad (1)$$

where N_V , k_B , and T is effective density of states, Boltzmann constant, and temperature, respectively.

We continue to systematically investigate the electrical properties of the NiO_x film upon modification. We calculate the defect density (n_t) and hole mobility (μ_p) of the NiO_x and $\text{NiO}_x\text{:TTTS}$ films via the space-charge-limited current method in **Figure 2c** where the inset is the device structure. The curve is divided into three regions with the increase of bias. The ohmic region of linear behavior appears at low voltage, while it will transit to the trap-filling region when current increases nonlinearly caused by totally filled trap states. This critical trap-filled limit voltage (V_{TFL}) can be used for n_t calculation via the formula^[30]:

$$V_{TFL} = \frac{qn_t L^2}{2\epsilon\epsilon_0} \quad (2)$$

where q and L is elementary charge (1.6×10^{-19} C) and the NiO_x layer thickness (20 nm), respectively. ϵ and ϵ_0 is relative permittivity (11.9 for NiO_x) and vacuum permittivity, respectively. The calculated n_t is $1.97 \times 10^{18} \text{ cm}^{-3}$ for $\text{NiO}_x\text{:TTTS}$ film, which is lower than NiO_x film ($2.70 \times 10^{18} \text{ cm}^{-3}$), indicating that TTTS can effectively passivate defects such as O dangling bonds in the pristine NiO_x film and obtain better electrical performance. As the bias continues to increase, there is a region with typical quadratic voltage dependence where it is the trap-free region. The μ_p can be calculated via Mott-Gurney law^[31]:

$$J = \frac{9\epsilon\epsilon_0\mu_p V_b^2}{8L^3} \quad (3)$$

where V_b and J is applied voltage and current density, respectively. The calculated μ_p increases from 8.3×10^{-7} (NiO_x) to $2.3 \times 10^{-6} \text{ cm}^2 \text{ v}^{-1} \text{ s}^{-1}$ ($\text{NiO}_x\text{:TTTS}$), revealing better charge transport and less

recombination. In **Figure 2d**, the conductivity can be calculated via the following formula^[32]:

$$J = \frac{\sigma V}{L} \quad (4)$$

The conductivity of the NiO_x:TTTS film enhances to $2.5 \times 10^{-5} \text{ S cm}^{-1}$, which is 4.2 times than the pristine NiO_x film (note: this is confirmed via the formula: $\sigma = \mu_p q p$). Therefore, the better electrical property of the NiO_x film indicates an enhanced hole density, hole mobility, conductivity as well as reduced defect density.^[27]

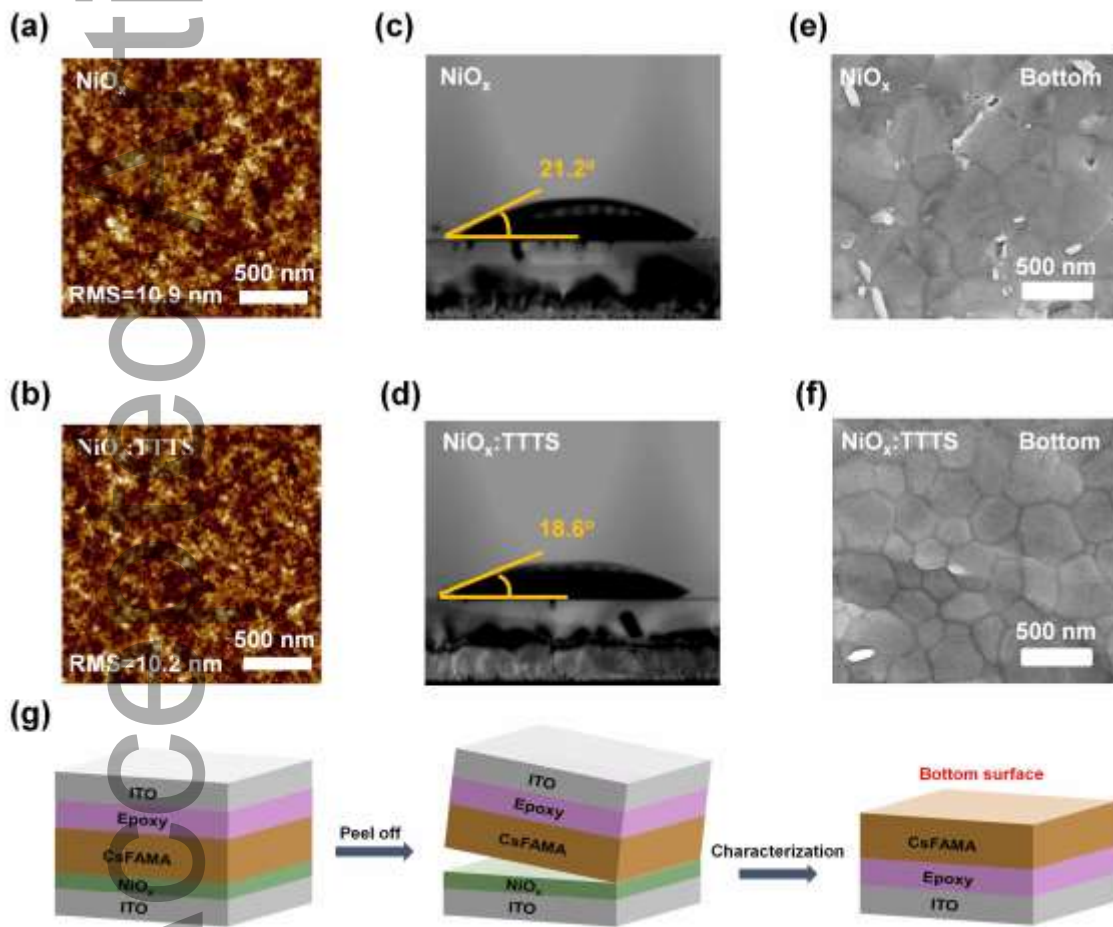


Figure 3. Surface morphology and optical properties. The AFM images of NiO_x film (a) without or (b) with TTTS. The contact angle changes of the (c) NiO_x and (d) NiO_x:TTTS films. The SEM images of bottom surface for perovskite film based on (e) NiO_x and (f) NiO_x:TTTS films. (g) The preparation process of b-CsFAMA film for SEM characterization.

Besides the excellent electrical properties, TTTS has a good effect on the improvement of surface topography of the NiO_x layer. Atomic force microscope (AFM) is employed to measure the

root-mean-square (RMS) surface roughness of the NiO_x films. AFM images (**Figure 3a and b**) exhibit that the RMS roughness slightly reduces from 10.9 to 10.2 nm after TTTS modification, which is beneficial for perovskite deposition.^[21] In addition, **Figure 3c and d** depict the contact angle changes of water droplets on NiO_x and NiO_x:TTTS films. The contact angle of water is 21.2° for the NiO_x film, while it reduces to 18.6° for the NiO_x:TTTS film, which is more favorable for heterogeneous nucleation and preparation of high-quality CsFAMA film^[33]. Therefore, we examine the scanning electron microscope (SEM) images of top (**Figure S6**) and bottom (**Figure 3e and f**) surface for CsFAMA films (termed as t- and b-CsFAMA film, respectively) to observe the surface morphology of CsFAMA films. There is no obvious change for the t-CsFAMA film in **Figure S6**. The b-CsFAMA film can be obtained via peeling off the CsFAMA film with epoxy as shown in **Figure 3g**^[34]. Many pinholes and residual lead iodide at grain boundaries can be observed from the b-CsFAMA film deposited on the pristine NiO_x layer. On the contrary, dense and smooth b-CsFAMA film is obtained after the TTTS modification, which could be attributed to the flatter substrate and reduced free energy of heterogeneous nucleation.^[33] As shown in **Figure S7**, the better optical property is confirmed from the slightly enhanced Ultraviolet-Visible (UV-Vis) absorption spectrum of NiO_x:TTTS /CsFAMA film. Moreover, to eliminate the influence of the substrate on light absorption, we measure the transmittance of NiO_x film from UV-Vis absorption spectra in **Figure S8**. The transmittance of modified NiO_x film is as high as pristine NiO_x film, indicating that film still maintains a good transmittance.

To evaluate the effect of NiO_x:TTTS film on device performance, we prepare the fully structured PSCs based on NiO_x film without or with TTTS additive in **Figure 1a**. The devices with different concentrations of TTTS are prepared and characterized via the *J-V* curves in **Figure S9**. The

champion device with 0.8% mg mL⁻¹ of TTTS in NiO_x film is termed as NiO_x:TTTS device and its detailed parameters are given in **Table S1**. The reverse (forward) scan and detailed parameters are recorded in **Figure 4a** and **Table 1**, which is consistent with our previous report.^[35] The Control device displays a relative low V_{OC} of 1.11 (1.10) V, J_{SC} of 22.53 (21.89) mA cm⁻² and FF of 80.40% (79.47%), thence an unsatisfactory PCE of 20.12% (19.20%). On the contrary, an improved PCE of 22.81% (22.13%) is observed in NiO_x:TTTS device with enhanced V_{OC} 1.15 (1.14) V, J_{SC} 23.49 (23.15) mA cm⁻² and FF 84.68% (83.84%). Moreover, the calculated hysteresis index (HI) of devices reduces from 4.6% to 3.0% after TTTS modification.

Table 1. The detailed photoelectric performance of inverted PSCs based on NiO_x or NiO_x:TTTS layer.

Device [mg mL ⁻¹]		V_{OC} [V]	J_{SC} [mA cm ⁻²]	FF [%]	PCE [%]	HI ^c [%]	R_s [Ω cm ²]	R_{sh} [Ω cm ²]
Control	F ^a	1.10	21.89	79.74	19.20	4.6	8.51	3567
	R ^b	1.11	22.53	80.40	20.12			
0.8 %	F ^a	1.14	23.15	83.84	22.13	3.0	3.52	12001
	R ^b	1.15	23.49	84.68	22.81			

^a The forward scan direction.

^b The reverse scan direction.

^c $HI = (PCE_{reverse} - PCE_{forward}) / PCE_{reverse}$.^[36]

In addition, the TTTS modified device displays excellent repeatability attributed to lower standard deviation from the device statistics (**Figure S10**). We continue to perform the steady-state photocurrent and stabilized power output (SPO) at the maximum power point (MPP) in **Figure 4b** for Control and NiO_x:TTTS device (the MPP is 0.89 and 0.98 V, respectively). The optimized device retains a higher and stable SPO contrasted with a slightly decreased SPO of the Control device. In **Figure 4c**, we perform the external quantum efficiency (EQE) spectrum, where the NiO_x:TTTS device displays higher EQE over the whole wavelength region leading to enhanced integrated J_{SC} . In

addition, the integrated J_{SC} of Control and NiO_x :TTTS device (20.59 and 22.60 mA cm^{-2} , respectively) is consistent with the J - V characterization. Moreover, we fabricate a large area device (1 cm^2) via blade coating and anti-immersion method and obtain a champion PCE of 20.18% , revealing that our strategy is suitable for preparation of larger area devices (**Figure S11**).

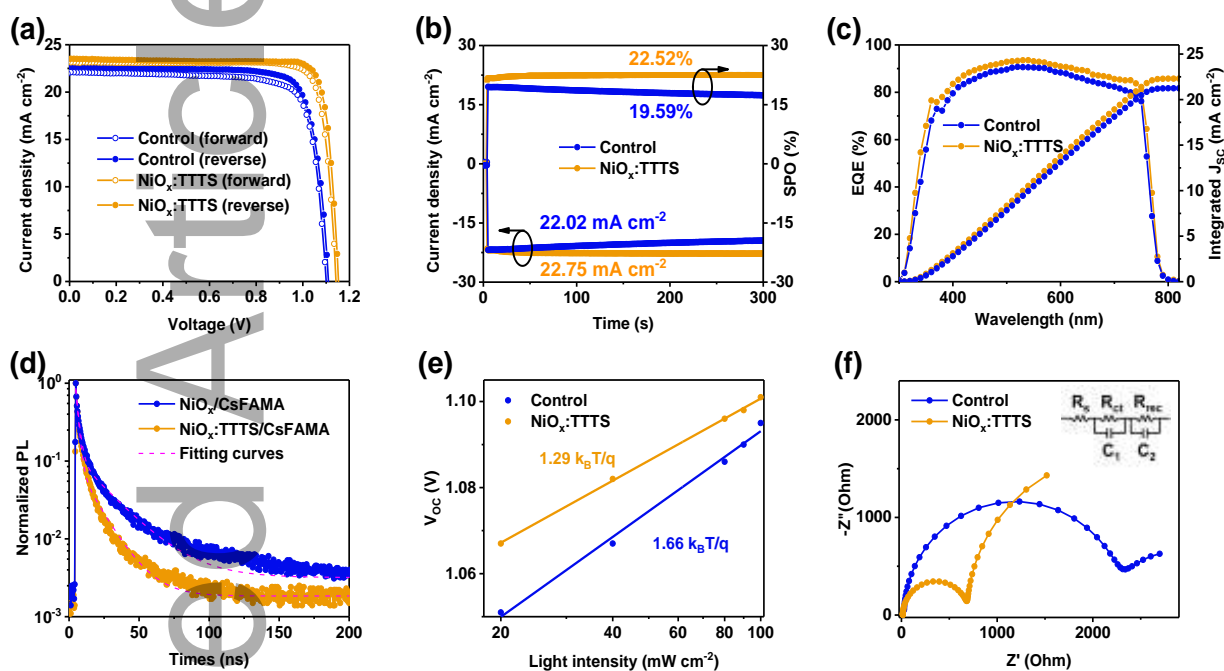


Figure 4. Photoelectric performance and electrical properties of NiO_x and NiO_x :TTTS devices. (a) The J - V curves at forward and reverse scan direction. (b) The steady-state photocurrent and SPO. (c) The EQE and integrated J_{SC} . (d) The time-resolved PL decay of the CsFAMA film with NiO_x or NiO_x :TTTS layer. (e) V_{OC} dependence on light intensity. (f) The Nyquist plots in dark condition with the equivalent circuit in inset.

To investigate the better photoelectric performance of the optimized device, we mainly conduct internal electrical properties of the PSCs because the better light absorption of optimized device has been discussed in **Figure 3g**. Steady-state photoluminescence (PL) and time-resolved PL (TRPL) characterizations are performed to investigate the carrier extraction and transport via depositing CsFAMA film based on NiO_x or NiO_x :TTTS layer. As shown in **Figure S12**, the CsFAMA film based on NiO_x :TTTS layer displays more effective PL quenching, which reveals better hole extraction and transport after the TTTS modification^[37]. Therefore, we continue to calculate the carrier lifetime (τ)

in **Table S2** via bi-exponential decay functions to fit the TRPL results (**Figure 4d**). Compared to the

Control device ($\tau_{\text{avg}} = 5.33$ ns), the carrier lifetime of the NiO_x:TTTS device is reduced to 2.66 ns, indicating that the photogenerated carriers can be effectively extracted from the CsFAMA layer to the NiO_x:TTTS layer, thus resulting in an increased J_{SC} .

To better understand the excellent electrical properties of the optimized devices, we conduct the V_{OC} (**Figure 4e**) and J_{SC} (**Figure S13**) under various light intensity (I). The relationship between V_{OC} and light intensity can be calculated by the following equation^[38]: $V_{\text{OC}} \propto n(k_B T/q) \ln(I)$, where n represent the ideality factor. The NiO_x:TTTS device shows a small ideality factor of 1.29 compared with the Control device (1.66), which indicates reduced trap-assisted recombination in the NiO_x:TTTS device. This can be confirmed by dark J - V characterization (**Figure S14**). The lower leakage current reveals a more efficient electron extraction rather than recombined in the NiO_x:TTTS device^[39]. We further calculate the series resistances (R_s) and shunt resistances (R_{sh}) of the devices listed in **Table 1**. To inspect the extract transfer resistance in devices, we further perform the electrochemical impedance spectroscopy (EIS), as shown in **Figure 4f**. The charge transport resistance (R_{ct}) value is obtained from the high-frequency region of the Nyquist plots, which is 2370 and 695 Ω for Control and NiO_x:TTTS devices, respectively. The recombination resistance (R_{rec}) value refers to the low-frequency of the Nyquist plots, which is 1480 and 3330 Ω for Control and NiO_x:TTTS devices, respectively. The optimized device displays smaller R_{ct} and larger R_{rec} compared with that of the Control device, indicating an improvement in electron transport, inhibition in charge recombination, thus leading to an enhanced FF^[40]. Overall, we attributed such excellent electrical properties of the NiO_x:TTTS device to its suitable band alignment, enhanced conductivity as well as the improved interfacial contact.

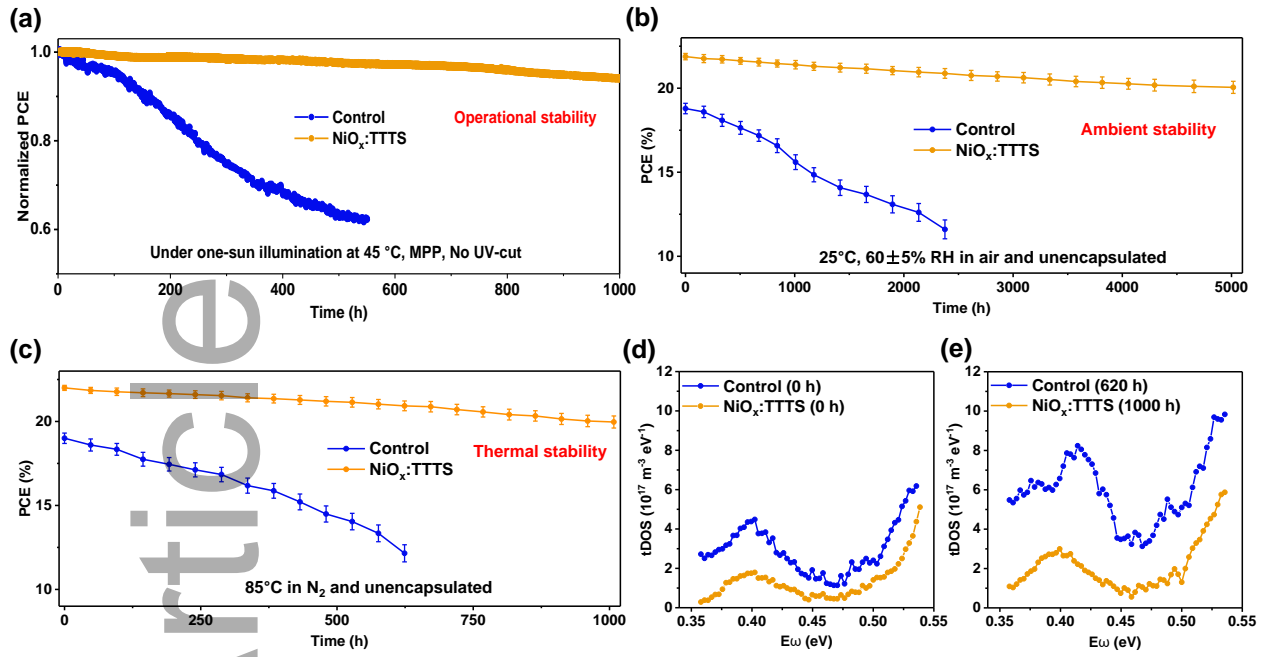


Figure 5. Stability characterization of Control and NiO_x:TTTS devices. (a) Operational stability test of encapsulated devices under one-sun illumination without UV filter at to track the MPP 45 °C. The normalized SPO value is the degradation trace from a single champion device. (b) The ambient stability test of unencapsulated devices in air (25 °C, 60 ± 5% RH). (c) Thermal stability test of unencapsulated devices at 85 °C in a N₂-filled glovebox. The average PCE and standard error are calculated from ten devices. The tDOS curves of Control and NiO_x:TTTS devices (d) before and (e) after thermal stability test.

To investigate the resistance of the TTTS-modified devices to illumination, moisture, and thermal, we carry out a series of stability tests. As shown in **Figure 5a**, the operational stability is performed via soaking the champion encapsulated devices in continuous one-sun illumination at 45 °C to track MPP. The NiO_x:TTTS device retains 94% of its initial SPO after 1000 h, while the Control device losses around 40% after 550 h. We continue to monitor the ambient stability of the unencapsulated devices at 25 °C and 60 ± 5% RH. The optimized devices maintain 92% of its initial PCE after 5000 h, whereas the Control devices just retain 62% after 2400 h. The thermal stability of the unencapsulated devices is performed in a nitrogen atmosphere at 85 °C for 1000 h. The devices based on NiO_x:TTTS film still maintain 91% of its initial PCE after 1000 h, and the Control devices only retain 64% after 620 h.

To investigate the mechanism of the improved stability, we conduct trap density of states (tDOS) measurement on the fresh devices and aged devices after thermal stability test. The tDOS values can be calculated from the following equation^[41]:

$$N_T(E_\omega) = - \frac{V_{bi}}{qW} \frac{dC}{d\omega} \frac{\omega}{k_B T} \quad (5)$$

where W is the depletion, C is the capacitance, and V_{bi} is the built-in potentials from the Mott-Schottky plots (**Figure S15**). The energy demarcation (E_ω) is calculated via attempt-to-escape frequency (ω_0) and applied angular frequency (ω)^[41]:

$$E_\omega = k_B T \ln \frac{\omega_0}{\omega} \quad (6)$$

According to the previous report, the shallower traps (0.35-0.4 eV) are attributed to defects in grain boundaries, while the deeper traps (0.4-0.52 eV) are originated from the surface defects^[42]. As for the fresh devices, the NiO_x:TTTS device displays lower tDOS values than the Control device over the entire energy demarcation, which can be attributed to the reduced defect density of the NiO_x film and better crystallinity of the CsFAMA film. The reduced interface defect density leads to ameliorated interface contact, inhibiting perovskite degradation, which improves device stability.^[43] After the thermal stability test under continuous heating at 85 °C in nitrogen, the Control device displays significantly increased tDOS values, revealing irreversible degradation of the CsFAMA perovskite caused by the poor bottom interface contact with the NiO_x layer, which has been dramatically improved upon TTTS treatment. As a result, the optimized device maintains similar tDOS values before and after ageing. In addition, better conductivity of NiO_x:TTTS layer can enhance charge extraction, which can depress interfacial charge accumulation and enhance device stability.^[18]

3. Conclusion

We introduce TTTS into the NiO_x layer via a simple additive engineering to achieve efficient and stable PSCs. The strong coordination bond between N in TTTS and Ni²⁺ in NiO_x contributes to increase the ratio of Ni³⁺: Ni²⁺, thus enhancing the conductivity and hole extraction ability of the NiO_x film. In addition, the O-Na bond is beneficial to reduce defect density. Moreover, the TTTS additive helps to improve the crystallinity of the CsFAMA film and reduce the charge recombination at the NiO_x /CsFAMA interface. Eventually, the target device achieves a champion PCE of 22.81% with excellent operational, ambient and thermal stabilities. The optimized device keeps 94% of its initial SPO under continuous one-sun illumination at MPP for 1000 h, maintains 92% in ambient air at 25 °C and 60 ± 5% RH for 5000 h, and 91% in nitrogen for 1000 h at 85 °C, respectively. More importantly, our work provides a facile additive engineering strategy to treat the NiO_x layer toward efficient and stable inverted PSCs.

Acknowledgements

This research is supported by the National Natural Science Foundation of China (52172237, 52072228), the Shaanxi International Cooperation Project (2020KWZ-018), the Shaanxi Science Fund for Distinguished Young Scholars (2022JC-21), the Research Fund of the State Key Laboratory of Solidification Processing (NPU), China (Grant No. 2021-QZ-02), and the Fundamental Research Funds for the Central Universities (3102019JC005, D5000220033). We thank the members from the Analytical & Testing Center of Northwestern Polytechnical University for the help of UPS, XRD, and SEM characterization.

Declaration of Competing Interest

The authors declare no competing financial interest.

This article is protected by copyright. All rights reserved

References

- [1] J. Jeong, M. Kim, J. Seo, H. Lu, P. Ahlawat, A. Mishra, Y. Yang, M. A. Hope, F. T. Eickemeyer, M. Kim, Y. J. Yoon, I. W. Choi, B. P. Darwich, S. J. Choi, Y. Jo, J. H. Lee, B. Walker, S. M. Zakeeruddin, L. Emsley, U. Rothlisberger, A. Hagfeldt, D. S. Kim, M. Grätzel and J. Y. Kim, Pseudo-halide anion engineering for α -FAPbI₃ perovskite solar cells, *Nature* **2021**, 592, 381-385.
- [2] J. J. Yoo, G. Seo, M. R. Chua, T. G. Park, Y. Lu, F. Rotermund, Y.-K. Kim, C. S. Moon, N. J. Jeon, J.-P. Correa-Baena, V. Bulović, S. S. Shin, M. G. Bawendi and J. Seo, Efficient perovskite solar cells via improved carrier management, *Nature* **2021**, 590, 587-593.
- [3] Z. Dai, K. Yadavalli Srinivas, M. Chen, A. Abbaspourtamijani, Y. Qi and P. Padture Nitin, Interfacial toughening with self-assembled monolayers enhances perovskite solar cell reliability, *Science* **2021**, 372, 618-622.
- [4] A. D. Taylor, Q. Sun, K. P. Goetz, Q. An, T. Schramm, Y. Hofstetter, M. Litterst, F. Paulus and Y. Vaynzof, A general approach to high-efficiency perovskite solar cells by any antisolvent, *Nat. Commun.* **2021**, 12, 1878.
- [5] National Renewable Energy Laboratory (NREL), Best Research-Cell Efficiency Chart, <https://www.nrel.gov/pv/assets/pdfs/best-research-cell-efficiencies-rev220126.pdf> (accessed: March 2022).
- [6] Z. Li, B. Li, X. Wu, A. Sheppard Stephanie, S. Zhang, D. Gao, J. Long Nicholas and Z. Zhu, Organometallic-functionalized interfaces for highly efficient inverted perovskite solar cells, *Science* **2022**, 376, 416-420.
- [7] L. Xu, X. Chen, J. Jin, W. Liu, B. Dong, X. Bai, H. Song and P. Reiss, Inverted perovskite solar cells employing doped NiO hole transport layers: A review, *Nano Energy* **2019**, 63, 103860.
- [8] M. Degani, Q. An, M. Albaladejo-Siguan, J. Hofstetter Yvonne, C. Cho, F. Paulus, G. Grancini and Y. Vaynzof, 23.7% Efficient inverted perovskite solar cells by dual interfacial modification, *Sci. Adv.* **2021**, 7, eabj7930.
- [9] X. Xu, X. Ji, R. Chen, F. Ye, S. Liu, S. Zhang, W. Chen, Y. Wu and W.-H. Zhu, Improving contact and passivation of buried interface for high-efficiency and large-area inverted perovskite solar cells, *Adv. Funct. Mater.* **2022**, 32, 2109968.
- [10] X. Yang, D. Luo, Y. Xiang, L. Zhao, M. Anaya, Y. Shen, J. Wu, W. Yang, Y.-H. Chiang, Y. Tu, R. Su, Q. Hu, H. Yu, G. Shao, W. Huang, T. P. Russell, Q. Gong, S. D. Stranks, W. Zhang and R. Zhu, Buried interfaces in halide perovskite photovoltaics, *Adv. Mater.* **2021**, 33, 2006435.
- [11] M. I. Hossain, A. K. M. Hasan, W. Qarony, M. Shahiduzzaman, M. A. Islam, Y. Ishikawa, Y. Uraoka, N. Amin, D. Knipp, M. Akhtaruzzaman and Y. H. Tsang, Electrical and optical properties of nickel-oxide films for efficient perovskite solar cells, *Small Methods* **2020**, 4, 2000454.
- [12] S. Zhang, H. Wang, X. Duan, L. Rao, C. Gong, B. Fan, Z. Xing, X. Meng, B. Xie and X. Hu, Printable and homogeneous NiO_x hole transport layers prepared by a polymer-network gel method for large-area and flexible perovskite solar cells, *Adv. Funct. Mater.* **2021**, 31, 2106495.
- [13] W. Chen, Y. Wu, Y. Yue, J. Liu, W. Zhang, X. Yang, H. Chen, E. Bi, I. Ashraful, M. Grätzel

- and L. Han, Efficient and stable large-area perovskite solar cells with inorganic charge extraction layers, *Science* **2015**, 350, 944-948.
- [14] W. Chen, F.-Z. Liu, X.-Y. Feng, A. B. Djurišić, W. K. Chan and Z.-B. He, Cesium doped niox as an efficient hole extraction layer for inverted planar perovskite solar cells, *Adv. Energy Mater.* **2017**, 7, 1700722.
- [15] Y. Wei, K. Yao, X. Wang, Y. Jiang, X. Liu, N. Zhou and F. Li, Improving the efficiency and environmental stability of inverted planar perovskite solar cells via silver-doped nickel oxide hole-transporting layer, *Appl. Surf. Sci.* **2018**, 427, 782-790.
- [16] G. Li, Y. Jiang, S. Deng, A. Tam, P. Xu, M. Wong and H. S. Kwok, Overcoming the limitations of sputtered nickel oxide for high-efficiency and large-area perovskite solar cells, *Adv. Sci.* **2017**, 4, 1700463.
- [17] Y. Wang, T. Mahmoudi and Y.-B. Hahn, Highly stable and efficient perovskite solar cells based on FAMA-perovskite-Cu:NiO composites with 20.7% efficiency and 80.5% fill factor, *Adv. Energy Mater.* **2020**, 10, 2000967.
- [18] Q. He, K. Yao, X. Wang, X. Xia, S. Leng and F. Li, Room-temperature and solution-processable Cu-doped nickel oxide nanoparticles for efficient hole-transport layers of flexible large-area perovskite solar cells, *ACS Appl. Mater. Interfaces* **2017**, 9, 41887-41897.
- [19] W. Chen, Y. Wu, J. Fan, A. B. Djurišić, F. Liu, H. W. Tam, A. Ng, C. Surya, W. K. Chan, D. Wang and Z.-B. He, Understanding the doping effect on NiO: Toward high-performance inverted perovskite solar cells, *Adv. Energy Mater.* **2018**, 8, 1703519.
- [20] J. H. Lee, Y. W. Noh, I. S. Jin, S. H. Park and J. W. Jung, A solution-processed cobalt-doped nickel oxide for high efficiency inverted type perovskite solar cells, *J. Power Sources* **2019**, 412, 425-432.
- [21] X. Wan, Y. Jiang, Z. Qiu, H. Zhang, X. Zhu, I. Sikandar, X. Liu, X. Chen and B. Cao, Zinc as a new dopant for NiO_x-based planar perovskite solar cells with stable efficiency near 20%, *ACS Appl. Energy Mater.* **2018**, 1, 3947-3954.
- [22] H. Bao, M. Du, H. Wang, K. Wang, X. Zuo, F. Liu, L. Liu, D. Eder, A. Cherevan, S. Wang, L. Wan, S. Zhao and S. Liu, Samarium-doped nickel oxide for superior inverted perovskite solar cells: Insight into doping effect for electronic applications, *Adv. Funct. Mater.* **2021**, 31, 2102452.
- [23] P. Ru, E. Bi, Y. Zhang, Y. Wang, W. Kong, Y. Sha, W. Tang, P. Zhang, Y. Wu, W. Chen, X. Yang, H. Chen and L. Han, High electron affinity enables fast hole extraction for efficient flexible inverted perovskite solar cells, *Adv. Energy Mater.* **2020**, 10, 1903487.
- [24] W. Chen, Y. Zhou, L. Wang, Y. Wu, B. Tu, B. Yu, F. Liu, H. W. Tam, G. Wang, A. B. Djurisić, L. Huang and Z. He, Molecule-doped nickel oxide: Verified charge transfer and planar inverted mixed cation perovskite solar cell, *Adv. Mater.* **2018**, 30, 1800515.
- [25] A. P. Grosvenor, M. C. Biesinger, R. S. C. Smart and N. S. McIntyre, New interpretations of XPS spectra of nickel metal and oxides, *Surf. Sci.* **2006**, 600, 1771-1779.
- [26] A. Seikhan, M. Neophytou, R. K. Hallani, J. Troughton, N. Gasparini, H. Faber, E. Abou-Hamad, M. N. Hedhili, G. T. Harrison, D. Baran, L. Tsetseris, T. D. Anthopoulos and I. McCulloch, A multilayered electron extracting system for efficient perovskite solar cells, *Adv. Funct. Mater.* **2020**, 30, 2004273.
- [27] L. Xie, Z. Cao, J. Wang, A. Wang, S. Wang, Y. Cui, Y. Xiang, X. Niu, F. Hao and L. Ding,

Improving energy level alignment by adenine for efficient and stable perovskite solar cells, *Nano Energy* **2020**, 74, 104846.

- [28] C. Hu, Y. Bai, S. Xiao, K. Tao, W. K. Ng, K. S. Wong, S. H. Cheung, S. K. So, Q. Chen and S. Yang, Surface sulfuration of nio boosts the performance of inverted perovskite solar cells, *Sol. RRL* **2020**, 4, 2000270.
- [29] S. Zhumagali, F. H. Isikgor, P. Maity, J. Yin, E. Ugur, M. De Bastiani, A. S. Subbiah, A. J. Mirabelli, R. Azmi, G. T. Harrison, J. Troughton, E. Aydin, J. Liu, T. Allen, A. u. Rehman, D. Baran, O. F. Mohammed and S. De Wolf, Linked nickel oxide/perovskite interface passivation for high-performance textured monolithic tandem solar cells, *Adv. Energy Mater.* **2021**, 11, 2101662.
- [30] J. Han, X. Pu, H. Zhou, Q. Cao, S. Wang, Z. He, B. Gao, T. Li, J. Zhao and X. Li, Synergistic effect through the introduction of inorganic zinc halides at the interface of TiO₂ and Sb₂S₃ for high-performance Sb₂S₃ planar thin-film solar cells, *ACS Appl. Mater. Interfaces* **2020**, 12, 44297-44306.
- [31] T. Li, S. Wang, J. Yang, X. Pu, B. Gao, Z. He, Q. Cao, J. Han and X. Li, Multiple functional groups synergistically improve the performance of inverted planar perovskite solar cells, *Nano Energy* **2021**, 82, 105742.
- [32] Q. Cao, Z. Li, J. Han, S. Wang, J. Zhu, H. Tang, X. Li and X. Li, Electron transport bilayer with cascade energy alignment for efficient perovskite solar cells, *Sol. RRL* **2019**, 3, 1900333.
- [33] Y. Li, M. Dailey, P. J. Lohr and A. D. Printz, Performance and stability improvements in metal halide perovskite with intralayer incorporation of organic additives, *J. Mater. Chem. A* **2021**, 9, 16281-16338.
- [34] S. Chen, X. Dai, S. Xu, H. Jiao, L. Zhao and J. Huang, Stabilizing perovskite-substrate interfaces for high-performance perovskite modules, *Science* **2021**, 373, 902-907.
- [35] S. Wang, Y. Li, J. Yang, T. Wang, B. Yang, Q. Cao, X. Pu, L. Etgar, J. Han, J. Zhao, X. Li and A. Hagfeldt, Critical role of removing impurities in nickel oxide on high-efficiency and long-term stability of inverted perovskite solar cells, *Angew. Chem. Int. Ed.* **2022**, 61, e202116534.
- [36] X. Pu, J. Han, S. Wang, H. Zhou, Q. Cao, J. Yang, Z. He and X. Li, Surface modification with ionic liquid for efficient CsPbI₂Br perovskite solar cells, *J. Materiomics* **2021**, 7, 1039-1048.
- [37] B. Gao, Q. Cao, X. Pu, J. Yang, J. Han, S. Wang, T. Li, Z. He and X. Li, Bi-Directional functionalization of urea-complexed SnO₂ for efficient planar perovskite solar cells, *Appl. Surf. Sci.* **2021**, 546, 148711.
- [38] S. Wang, X. Li, T. Tong, J. Han, Y. Zhang, J. Zhu, Z. Huang and W. C. H. Choy, Sequential processing: Spontaneous improvements in film quality and interfacial engineering for efficient perovskite solar cells, *Sol. RRL* **2018**, 2, 1800027.
- [39] J. Han, X. Pu, H. Zhou, Q. Cao, S. Wang, J. Yang, J. Zhao and X. Li, Multidentate anchoring through additive engineering for highly efficient Sb₂S₃ planar thin film solar cells, *J. Mater. Sci. Technol.* **2021**, 89, 36-44.
- [40] Q. Cao, Y. Li, H. Zhang, J. Yang, J. Han, T. Xu, S. Wang, Z. Wang, B. Gao, J. Zhao, X. Li, X. Ma, S. M. Zakeeruddin, W. E. I. Sha, X. Li and M. Grätzel, Efficient and stable inverted perovskite solar cells with very high fill factors via incorporation of star-shaped polymer, *Sci. Adv.* **2021**, 7, eabg0633.
- [41] S. Wang, B. Yang, J. Han, Z. He, T. Li, Q. Cao, J. Yang, J. Jiajia, X. Li, Z. Liu, S. F. Liu, C.

Tang and A. Hagfeldt, Polymeric room-temperature molten salt as multiple functional additive toward highly efficient and stable inverted planar perovskite solar cells, *Energy Environ. Sci.* **2020**, 13, 5068-5079.

- [42] Y. Bai, Y. Lin, L. Ren, X. Shi, E. Strounina, Y. Deng, Q. Wang, Y. Fang, X. Zheng, Y. Lin, Z.-G. Chen, Y. Du, L. Wang and J. Huang, Oligomeric silica-wrapped perovskites enable synchronous defect passivation and grain stabilization for efficient and stable perovskite photovoltaics, *ACS Energy Lett.* **2019**, 4, 1231-1240.
- [43] B. Zhang, J. Su, X. Guo, L. Zhou, Z. Lin, L. Feng, J. Zhang, J. Chang and Y. Hao, NiO/perovskite heterojunction contact engineering for highly efficient and stable perovskite solar cells, *Adv. Sci.* **2020**, 7, 1903044.

Accepted Article

Journal's Table of Contents

We have introduced the trimercapto-s-triazine trisodium salt (TTTS) in NiO_x layer. The TTTS can coordinate with Ni^{2+} in NiO_x via electron-deficient triazine ring to increase the concentration of Ni^{3+} and intrinsic conductivity of NiO_x . The modified device achieves the best PCE of 22.81% and excellent operational, ambient and thermal stabilities.

